ACS APPLIED MATERIALS & INTERFACES

Research Article

www.acsami.org

Shape Dependent Synthesis and Field Emission Induced Rectification in Single ZnS Nanocrystals

Umamahesh Thupakula, Amit Dalui, Anupam Debangshi, Jayanta K. Bal, Gundam S. Kumar, and Somobrata Acharya*

Centre for Advanced Materials, Indian Association for the Cultivation of Science, Kolkata 700032, India

Supporting Information

ABSTRACT: We report on the synthesis of shape controlled ZnS nanocrystals designed into nanodots, nanorods, and nanowires retaining the same diameter and crystallographic phase. We used UHV scanning tunneling microscopy and spectroscopy to study rectification behavior from single nanocrystals. The nanorod and nanowire show large tunneling current at the negative bias in comparison to the positive bias demonstrating current rectification, while the nanodot shows symmetric current−voltage behavior. We proposed a tunneling mechanism where direct tunneling is followed by resonant tunneling mechanism through ZnS nanocrystal at lower applied bias voltages. Stimulation of field emission in Fowler−Nordheim tunneling regime at higher negative bias voltages enables the rectification behavior from the ZnS nanorod or nanowire. Absence of rectification from the ZnS nanodot is associated with spherical shape where the field emission becomes less significant. Realizing functional electronic component from such shape dependent single ZnS nanocrystal may provide a means in realizing nanocrystal based miniaturized devices.

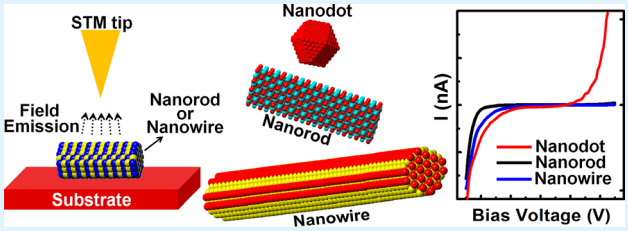

KEYWORDS: *shape dependent ZnS nanocrystals, scanning tunneling microscopy and spectroscopy, resonant tunneling, field emission, rectification*

INTRODUCTION

Shape dependent electronic properties of semiconductor nanocrystals are fundamentally important in establishing novel properties and for incorporating them for device fabrication.[1−4] It is well established that the quantum confinement effect is highly sensitive to the nanocrystal size in comparison to its exciton Bohr radius.[5,6] In addition, the effect of nanocrystal shape is also pronounced due to variable degrees of freedom for the charge carriers depending upon the shape.[7] A variety of novel aspects can be realized from the shape controlled nanocrystals. For example, a crossover in the valence levels upon changing the nanocrystal shape from zero-dimensional (0D) quantum dots to one-dimensional (1D) nanorods result in a change in the polarization properties of emitted light[8] or change in the shape modulates the degree of electron-phonon confinement.[7] Significant researches have been in progress towards the realization of field emission devices based on the size or shape controlled inorganic semiconductor nanocrystals due to its versatile use in commercial displays.[9−11] Designing high quality field emitters comprising the stability and low turn-on field for emission current remains a significant challenge.[12] 1D nanocrystals often show enhanced field emission properties associated with the aspect ratio.[13] The conventional field emission setup also makes use of bulk electrodes (with tip electrode cross section area varying from ∼mm^2 to ∼μm^2), which restricts the inherent phenomena of field emission properties from single nanocrystal.[14] The crystallographic facets which are contributing to the growth, crystalline quality and radius of curvature at the tips of the nanocrystals play crucial role in field emitting properties.[15] Moreover, the nanostructures with high aspect ratio or vertically aligned nanostructures with high packing density are proven to be vital for improved field emission properties.[13] Even though vertically aligned structures enhance the field emission properties, the minimum achievable radius at the edge of the tips (few tens of nanometers) limits the improved field emitting properties. Exploring newly designed single nanocrystal preferentially in horizontal configuration for field emission properties encompass multi-functionality along this direction.

In this context, an advanced tool such as scanning tunneling microscopy and spectroscopy (STM and STS) surpass the limitations imposed by bulk electrodes by probing the properties at the nanometer scale resolution.[16] The combination of imaging and tunneling spectroscopy using STM reveals single particle density of states from semiconductor nanocrystal owing to the resonant tunneling of electrons through discretized conduction and valence bands.[17−19] The concept of making the rectifier in STM depends on the formation of asymmetric double barrier tunnel junction (DBTJ) and also on the relative positions of valence band and conduction band of the nanocrystal under characterization.[20] Additionally, cross

Received: February 25, 2014
Accepted: April 29, 2014
Published: April 29, 2014

over from resonant tunneling to field emission in Fowler–Nordhiem (FN) tunneling regime may account the excess charge carrier tunneling at relatively higher applied voltages.[21,22] Thus, a proper choice of material, which enables field emission perspectives in bulk counterpart, might be advantageous in realizing single nanocrystal based rectifier. Here, we report on the synthesis of shape controlled zinc sulfide (ZnS) nanocrystals and shape dependent current rectification behavior using the STM and STS technique. ZnS is an important direct wide band gap (3.7 eV) semiconductor with a wide variety of potential applications in optoelectronic devices, sensors, and field emitting displays.[23−27] The rectifying behavior is observed from the tunneling spectra of ZnS nanorod and nanowire showing higher current in the negative bias compared to positive bias. In contrast, single ZnS nanodot does not exhibit rectification behavior showing symmetric current (I)−voltage (V) behavior at both the bias. We show that the rectification is primarily occurred via tunneling through the discrete energy levels of the nanorod or nanowire and field emission in FN tunneling regime provide a means for the large tunneling current at higher negative bias voltages. These observations points out to the role of nanocrystal shape on the rectification behavior from a single nanocrystal.

EXPERIMENTAL METHODS

Materials. 1-octylamine (OA, 90%), hexadecylamine (HDA, 90%), trioctylphosphine (TOP, 90%), methanol, and chloroform are purchased from Sigma-Aldrich. Shape controlled synthesis of ZnS nanocrystals are performed by thermal decomposition of single molecular precursor "zinc ethylxanthate" in mixed surfactants (TOP and HDA for nanodots, OA and HDA for nanorods and nanowires). Synthesis of zinc ethylxanthate is reported earlier.[4,28] Control over shapes retaining the same diameter of ZnS nanocrystals have been achieved by varying the precursor concentration, capping ligands, and annealing temperature.

Synthesis of ZnS Nanodots. ZnS nanodots of ∼3.5 nm in diameter are synthesized in one step under nitrogen gas flow by adding the zinc ethylxanthate (0.32 mM) into TOP (9 mM) at 75 °C. The resulting solution was added in one shot injection to the mixture of HDA and TOP (1:2 in molar ratio), which is maintained at 200 °C and then annealed for 10 min. Finally, the reaction mixture was cooled to 65 °C, where the excess surfactants are removed by adding methanol and chloroform (3:1 volume ratio) and centrifuging at 3000 rpm for 5 min. We have repeated this purification step for five times to remove the excess surfactants present in the sample. The residue was collected, dried under vacuum and stored in powder form for further characterization. Larger sized nanodots (∼9 ± 1 nm in diameter) have been synthesized by increasing the zinc ethylxanthate concentration (0.64 mM) and annealing time (60 min) while retaining all other parameters same as that of smaller sized dots.

Synthesis of ZnS Nanorods. Synthesis of ZnS nanorods are performed by adding zinc ethylxanthate (0.32 mM) into OA (12 mM) at 75°C in one step under nitrogen gas flow. Yellowish color appears immediately indicating the decomposition of zinc ethylxanthate. The resulting solution was added in one shot injection to HDA (8 mM), which is maintained at 200 °C and then annealed for 6 h at the same temperature.

Synthesis of ZnS Nanowires. ZnS nanowires are synthesized by increasing the concentration of zinc ethylxanthate (0.8 mM) and decreasing the annealing temperature to 190 °C and annealing for 6 h retaining all other parameters same as that of nanorods.

Characterization. Transmission electron microscopy (TEM) and high resolution TEM (HRTEM) measurements were carried out using a JEOL JEM-2010 microscope with an accelerating voltage of 200 kV. The sample was prepared by drop casting the nanocrystals from chloroform solution onto a lacey carbon coated copper electron microscope grid prior to TEM measurements. X-ray diffraction (XRD) patterns of all the samples were carried out using Bruker AXS: D8 advanced X-ray diffractometer with Cu Kα radiation (1.5418 Å). UV–vis absorption spectra were recorded with a Shimadzu UV-2550 spectrometer. STM and STS measurements were performed in ultrahigh vacuum ($\lesssim 3 \times 10^{-10}$ mbar) at room temperature (22 °C) with VT-SPM machine from Omicron Nanotechnology. For STM and STS measurements, the sample was prepared by drop casting the ZnS nanocrystals from chloroform solution on top of highly oriented pyrolytic graphite (HOPG) substrate. The I–V curves on isolated single ZnS nanocrystal are measured by disabling the feedback controls. Typically ∼50 I–V curves were averaged for each set-parameter to improve the signal to noise ratio.

RESULTS AND DISCUSSION

The TEM images of as synthesized ZnS nanodots, nanorods, and nanowires reveal that the smaller sized dots are of ∼3.5 ± 0.2 nm (Supporting Information, Figure S1), bigger sized dots are of ∼9 ± 1 nm in diameter, nanorods are of ∼20 nm in length and 3.5 ± 0.2 nm in diameter, and nanowires are of ∼50–60 nm in length and 3.5 ± 0.2 nm in diameter (Figure 1a–c). The aspect ratio, a parameter which defines length to

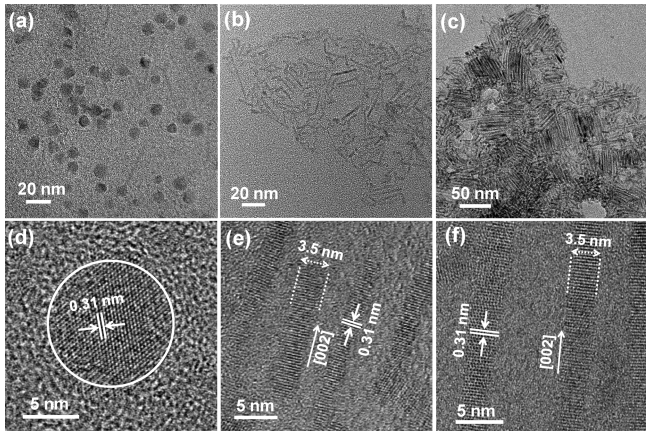

Figure 1. TEM images showing the size uniformity of ZnS (a) nanodot, (b) nanorod, and (c) nanowire. HRTEM image showing the lattice planes of a single ZnS (d) nanodot, (e) nanorod, and (f) nanowire corresponding to the (002) d-spacing's of bulk wurtzite crystallographic phase. The lattice spacing's diameter and growth directions are indicated in the figure.

diameter ratio of nanostructures, of nanowires is three (∼3) times longer than the nanorods. The corresponding HRTEM images of different shaped nanocrystals (Figure 1d–f, Supporting Information, Figure S1) reveal well resolved lattice planes with an inter-planar distance of ∼0.31 ± 0.02 nm consistent with the (002) d-spacing's of bulk wurtzite ZnS structure. The HRTEM images display high degree of crystallinity for all three different shapes of ZnS nanocrystals (Figure 1d–f). The observed lattice spacing's calculated from the statistical line profile analysis of HRTEM images (Supporting Information, Figure S2) supports (002) planes of bulk wurtzite ZnS. The HRTEM images of ZnS nanorods and nanowires indicate that the [002] crystallographic axis is parallel to the long axis of the nanorods and nanowires (Figure 1e and f). Note that the crystallographic phase of the nanodots, nanorods, and nanowires are same. The structural confirmations in wurtzite crystallographic phase of shape controlled ZnS nanocrystals is further supported by powder XRD patterns for nanodots, nanorods, and nanowires (Figure 2a). The highest intensity peak observed for (002) planes for the nanorods and

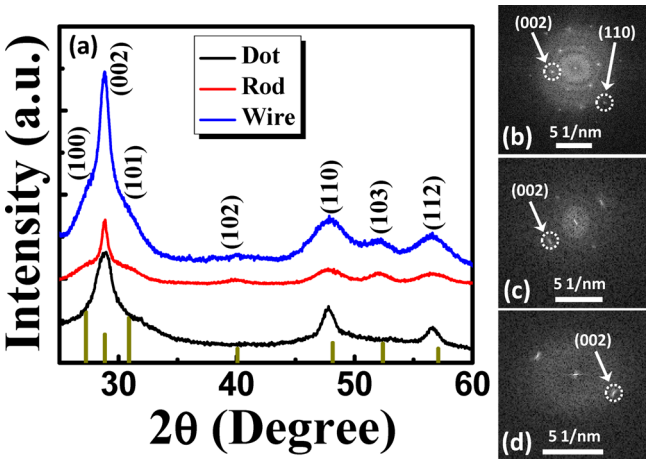

Figure 2. (a) Powder XRD patterns of ZnS nanodots (black curve), nanorods (red curve), and nanowires (blue curve) showing the peaks of Bragg's reflections. The peak positions are in line with that of the standard JCPDS power diffraction file #800007 (dark yellow vertical bars). FFT pattern generated from a single ZnS (b) nanodot, (c) nanorod, and (d) nanowire showing high intense spots (marked by dotted circle) originating from (002) planes.

nanowires suggesting the [002] growth direction (Figure 2a). Additional structural confirmations are provided by generating the Fast Fourier Transformation (FFT) from HRTEM image of an individual ZnS nanodot (Figure 2b), nanorod (Figure 2c), and nanowire (Figure 2d) using DM3 analysis software from JEOL. Comparison of FFT patterns of ZnS nanodot, nanorod, and nanowire reveal that the intensity of (002) spot becomes prominent as the shape changes from nanodots to nanowires (Figure 2b–d). Notably, the nanodots show multiple spots corresponding to different orientations of crystallographic planes in FFT, which are suppressed to (002) spots in case of nanorods and nanowires suggesting a specific growth direction. Intense spots of the (002) set of planes supports the growth direction along *c*-axis of wurtzite ZnS structure for nanorods and nanowires (Figure 2c and d).[29] Wurtzite ZnS is intrinsically anisotropic having zinc cationic plane at one end and sulfide anionic plane at the other side along *c*-axis. This leads to facile formation of nanorods or nanowires in the *c*-direction and induces essential chemical and electrostatic anisotropy in the nanorods or nanowires.[30] The band gap values are extracted from the UV–vis absorption spectra of ZnS nanodots (~3.76 eV), nanorods (~3.9 eV), and nanowires (~3.89 eV), which are larger than the bulk band gap of ZnS (~3.7 eV) suggesting the quantum confinement effect of charge carriers (Supporting Information, Figure S3).[5] There exists a close match in the band gap of ZnS nanodots with its bulk counterpart owing to its larger diameter (~9 ± 1 nm). Notably, the diameter of nanorod and nanowire is same (~3.5 nm) and the length of the nanowire is three (~3) times longer than the nanorod. The nearly same band gap values of ZnS nanorods and nanowires, hence, suggest that the diameter is the major confinement direction for these nanocrystals. Additionally, the smaller band gap value of ZnS nanodots in comparison to that of nanorods and nanowires indicating the lesser degree of confinement of charge carriers within the nanodots (Supporting Information, Figure S3).

The key to a precise shape control depends on the proper choice of surfactant ratios and reaction temperatures.[31−33] Control over aspect ratios by maintaining the same diameter (~3.5 nm) for both nanorods and nanowires have been achieved by varying the precursor concentration and annealing temperatures. The spherical nanodots have been obtained by using the TOP and HDA as capping ligands. We have used two different ligands (i.e., OA and HDA) to tune the shape from nanorods to nanowires, where OA was used as precursor solvent and HDA served as the main stabilizer of nanorods or nanowires. The use of amines as capping ligand has been shown to play an important role in determining the nanocrystal shape and growth.[28,31−35] The rapid injection of the precursors in OA results in the formation of a large number of ZnS seeds for which OA acts as a weak ligand. The alkyl amines are Lewis bases; the long alkyl chain length provides an increased electron density at the nitrogen site, thus inducing metal coordination. It is expected that due to its higher nucleophilic nature, HDA would replace OA to bind to zinc ions at the surface of nanorods or nanowires at an elevated temperature. Control experiments using only HDA or OA also lead to the ZnS wurtzite structures; however, the XRD peak intensities clearly confirm that a mixture of HDA and OA ligands plays the key role in tuning the size and shape of the ZnS nanorods or nanowires (Supporting Information, Figure S4).

The as-synthesized ZnS nanodots, nanorods, or nanowires are drop casted on HOPG substrate from chloroform solution and STM/STS measurements were carried out in ultra-high vacuum ($<3 \times 10^{-10}$ mbar) condition. The STM image of ZnS nanodots, nanorods, and nanowires reveals relatively larger dimensions with ~10–12 nm in diameter for nanodots, ~7 nm diameter and ~25 nm length of nanorods, and ~7 nm diameter and ~50–60 nm length of nanowires in comparison to the TEM images (Figure 3a–c). A finite radius of the STM tip may contribute to the apparent enlargement of nanocrystal dimensions.[36,37] Comparison of height profiles of the nanodot (~2.5 nm, inset of Figure 3a), nanorod (~4 nm, inset of Figure 3b), and nanowire (~1 nm, inset of Figure 3c) reveal that the magnitude of conductivity is lesser for nanowire in comparison to nanorod in spite of same diameter. Recall that ZnS nanowires are synthesized in mixed capping ligands (HDA and OA), where the nanowires are stabilized by these capping molecules. The adjacent nanowires within the dense assembly (Figure 3c) are separated by a bi-layer of capping molecules. These capping molecules are insulating in nature, which is detrimental for the conduction or tunneling. Hence, tunneling through the adjacent nanowires is unlikely because of the presence of bi-layer ligands, which offers higher tunneling resistance, rather tunneling through a single nanowire is feasible. The tunneling electrons could relax through the length of the nanowire, due to its increased degree of freedom for charge carriers along the length, which may reduce the net tunneling of electrons across the diameter resulting in the under estimation of height profile of a ZnS nanowire.[38] The tunneling spectra for nanodots, nanorods, and nanowires are taken with a fixed set-current and at different set-voltages. The *I*–*V* curves measured on a single isolated ZnS nanodot at set-current of 0.1 nA and at different set-voltages of 0.2, 0.4, and 0.8 V reveal symmetric behavior on either side of the zero-bias voltage (Figure 3d). However, the *I*–*V* curves measured on nanorods and nanowires reveal rectification features with low tunneling current in the positive bias and a large tunneling current in the negative bias (Figure 3e and f). The negative current sharply increases at higher negative bias voltages, with the electrons flowing from the substrate to tip. The asymmetry in the *I*–*V* curves between positive and negative bias voltages

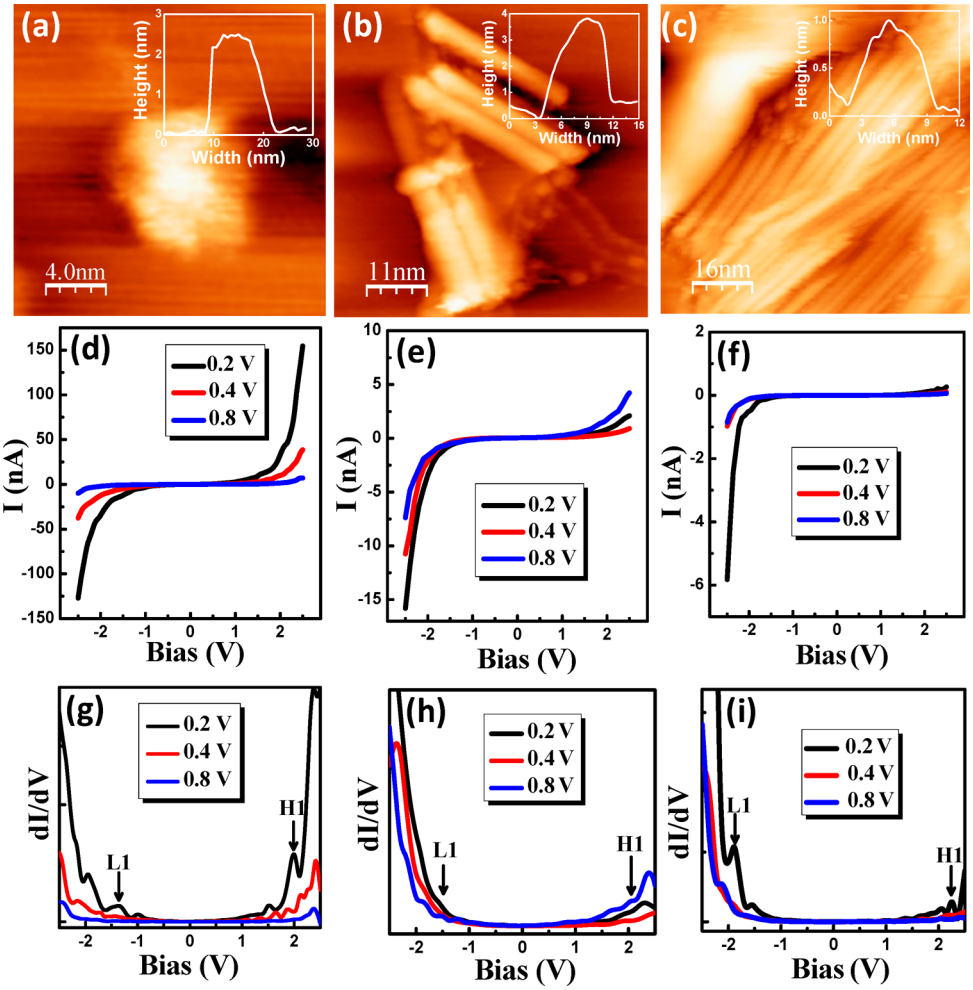

Figure 3. STM images showing (a) ZnS nanodots, (b) nanorods, and (c) nanowires on HOPG substrate. The STM images were obtained by using the set-voltage of 0.4 V and set-current of 0.1 nA. Inset of parts a–c: The line profiles showing the full width at half maximum corresponding to the width of a nanodot (~10–12 nm), nanorod (~7 nm), and nanowire (~7 nm). The *I*–*V* curves measured on a single isolated ZnS (d) nanodot, (e) nanorod, and (f) nanowire at three different set-voltages 0.2 V (black curve), 0.4 V (red curve), and 0.8 V (blue curve) at a fixed set-current of 0.1 nA. The corresponding d*I*/d*V* curves of (g) nanodot, (h) nanorod, and (i) nanowire calculated from the *I*–*V* curves. H1 at positive bias and L1 at negative bias denote the first valence and conduction level positions of ZnS nanocrystal, respectively.

gradually increases when the set-voltage decreased from 0.8 to 0.2 V at 0.1 nA set-current for both nanorod and nanowire (Figure 3e and f). This feature is not observed for nanodot (Figure 3d) indicating the absence of rectification behavior from the dots. The observed features suggest that the asymmetry in the voltage distribution in the vicinity of the nanorod or nanowire increases as the STM tip approaches closer to the nanorod or nanowire with the decrement of set-voltage. Additionally, the magnitude of current is found to be low for the nanowire in contrast to the nanorod at a fixed set-voltage and set-current suggesting the possible relaxation of tunneling electrons within the nanowire.[38] We have carried out the STM and STS measurements on ZnS nanodots of same diameter (~3.5 nm) as nanorod or nanowire as a control experiment, (see experimental section for synthesis details and Supporting Information, Figure S1), which exhibited insulating behavior. The insulating behavior may be associated with the increased band gap (~3.92 eV) due to the increased confinement for charge carriers in small sized nanocrystal (Supporting Information, Figure S5). Further control experiments on bare surface of HOPG substrate achieves the atomic resolution indicating the purity of STM tip and the corresponding STS measurements reveal symmetric *I*–*V* characteristics (Supporting Information, Figure S6) confirming that the rectification behavior is originating from the nanorod or nanowire itself.

The d*I*/d*V* spectra of ZnS nanodot, nanorod, and nanowire (Figure 3g–i) show peaks in the positive and negative bias on either side of the zero conductance region, bearing the signature of conduction and valence levels. The band gap is obtained from the difference of first peak positions at positive (H1) and negative (L1) bias in the d*I*/d*V* spectra reveals band gaps of 3.32, 3.5, and 3.5 eV for nanodot, nanorod, and nanowire, respectively. The band gaps measured from d*I*/d*V* spectra are somewhat lower than the band gaps calculated for nanodots, nanorods, and nanowires using UV–vis absorption spectroscopy. The lower band gap values observed in STS measurements may be assigned to the temperature effect as observed earlier for temperature dependent transport measurements on colloidal CdS rods.[39] Additionally, two low intense mid-gap peaks are observed just below the H1 and L1 in the band gap region of the d*I*/d*V* spectra. Such mid-gap peaks may be associated with the contribution of capping molecules present at the surfaces of the nanocrystal or from the defect

dx.doi.org/10.1021/am501165p | ACS Appl. Mater. Interfaces 2014, 6, 7856–7863

states present in the nanocrystals due to imperfect passivation of the capping molecules.[40−42] The energetic positions of the H1 and L1 peaks in dI/dV spectra are observed to be asymmetric with respect to the zero-bias. The minimum of conduction band and maximum of valence band of bulk ZnS are at −2.7 eV and −6.5 eV, respectively, relative to the vacuum level (Supporting Information, Figure S7), which confirms that the unoccupied conduction band minimum is closer to the Fermi levels of both tip ($E_{\text{F-Tip}}$, −4.5 eV for W[43]) and substrate ($E_{\text{F-HOPG}}$, −4.5 eV for HOPG[44]). Comparison of bulk band positions of ZnS with H1 and L1 positions from STS of ZnS nanodot/nanorod/nanowire indicates the contribution of valence level at positive bias and conduction level at negative bias. Within this framework, at negative bias, $E_{\text{F-HOPG}}$ become resonant with the discrete conduction levels of ZnS nanocrystal facilitating resonant tunneling of electrons from substrate to nanocrystal (Figure 3g−i). However, at positive bias, the electrons participate in the resonant tunneling from tip to substrate via discrete occupied levels of the nanocrystal indicating resonance of $E_{\text{F-HOPG}}$ with the valence levels of the nanocrystal (Figure 3g−i).

The observed rectification behavior could be explained from the asymmetric DBTJ formalism associated with the tip-nanocrystal-substrate configuration. Placing ZnS nanocrystal coated with capping ligand on HOPG substrate configures two different junctions at the tip-to-nanocrystal ($J_{\text{Tip-nanocrystal}}$) and nanocrystal-to-HOPG ($J_{\text{nanocrystal-HOPG}}$), respectively, forming DBTJ configuration while measuring in STM (Supporting information, Figure S8).[20,45] The asymmetric nature in both I−V and dI/dV curves around the zero bias voltage (Figure 3d−i) suggest an asymmetrical voltage distribution across the two junctions. The STM tip is expected to be in the closer proximity of the nanocrystal during tunneling condition as the STS measurements were performed at high set-currents and low set-voltages. Hence, most of the applied bias voltage drops at the $J_{\text{nanocrystal-HOPG}}$ junction and comparatively a lesser voltage drop is expected at $J_{\text{Tip-nanocrystal}}$ junction. Under this situation, the external bias voltage results in significant modification of $E_{\text{F-HOPG}}$ with respect to $E_{\text{F-Tip}}$ and also the inherent electronic levels of nanocrystal. Therefore, $E_{\text{F-HOPG}}$ sweeps through conduction and valence levels of the ZnS nanocrystal at negative and positive bias respectively revealing the signature of conduction and valence levels at negative and positive bias respectively in the dI/dV spectra (Figure 3g−i). Moreover, H1 and L1 peaks in the dI/dV curves show a small shift to higher bias voltages upon increasing the set-voltage from 0.2 to 0.8 V (Figure 3g−i). In the DBTJ configuration, an increase in the set-voltage by keeping the set-current constant moves the STM tip away from the nanocrystal. This increases the resultant voltage drop at $J_{\text{Tip-nanocrystal}}$ and simultaneously reduces the voltage drop at $J_{\text{nanocrystal-HOPG}}$. Such modification in the voltage drops at both the junctions alters the respective tunneling rates of the electrons/holes at the negative bias/positive bias. Additionally, the change in the tunneling rates of the charge carriers through the nanocrystal induces the charging effects which alter the peak positions in the dI/dV spectra.[46] The low intensity of the tunnel current at positive bias for nanorod or nanowire may be attributed to higher tunnel barrier associated with the tunneling of electrons while tunneling through the occupied valence levels of the nanorod or nanowire compared to the unoccupied conduction levels.[20,47] However, the above described resonant tunneling mechanism under DBTJ configuration is inadequate to explain the shape dependency of the rectification behavior and also the large asymmetry in the I−V curves at positive and negative bias of nanorods or nanowires. The combination of resonant tunneling and FN tunneling mechanisms together provide a possible explanation for the measured shape dependent electronic properties.

The resonant tunneling mechanism under DBTJ configuration may not be the sole contribution for the large rectification behavior observed for ZnS nanorods or nanowires. The large magnitude of tunneling current at negative bias, which is an indicative of tunneling of large number of charge carriers, could be associated with field emission from the nanorod or nanowire by considering the field emissive properties of ZnS.[11,23] We have plotted FN curves at negative bias in order to probe the field emission perspective for ZnS nanodot, nanorod, and nanowire. The FN curves reveal a logarithmic trend at low bias voltages indicating the direct tunneling of electrons through the nanocrystal (regime I, Figure 4a). An abrupt change in the tunneling behavior is observed for

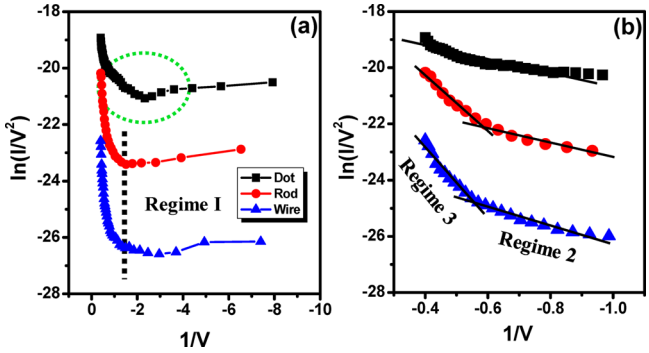

Figure 4. (a) FN plot at negative bias for ZnS nanodot (black squares and line), nanorod (red dots and line), and nanowire (blue up-triangles and line). A transition from logarithmic behavior (regime I) to apparent linear behavior is observed for nanorod and nanowire after a transition point (V_{trans}= −0.65 V, marked by black dotted line), which indicates a crossover from direct tunneling (regime I) to resonant and field emission regimes. The FN-plot of ZnS nanodot does not show sharp transition (rounded by green dotted ellipse) in the tunneling behavior. (b) Enlarged FN plot beyond the transition point for higher negative bias showing transition to resonant (regime II) and FN (regime III) tunneling regime for nanorod (red dots) and nanowire (blue up-triangles). Enlarged FN plot of ZnS nanodot (black squares) shows almost constant slope indicating the FN-tunneling mechanism is less dominating though the nanodot.

nanorod and nanowire after exceeding a critical voltage (V_{trans} = −0.65 V), revealing a crossover from the logarithmic to apparent linear behavior with negative slopes (Figure 4a). The FN plot of ZnS nanodot does not show such sharp rise rather a gradual change in the slope has been evidenced (Figure 4a). A close observation beyond V_{trans} of FN curves reveals two different slopes for nanorod and nanowire (labeled as regime II and regime III in Figure 4b). In the contrary, the FN curve of nanodot shows a continuous slope (Figure 4b). In particular, regime II of FN curves for nanorod or nanowire energetically fall into the resonant tunneling regime owing to the evolution of L1 peak in the dI/dV spectra in the same energetic position (Figure 3h and i). A sharp change in the tunneling behavior is observed immediately beyond regime II, which is associated with the FN tunneling of electrons through nanorod or nanowire (regime III, Figure 4b). However, such sharp rise in FN curve is not evidenced in case of nanodots suggesting the

FN tunneling mechanism is less significant possibly because of spherical shape of the ZnS nanocrystal. It clearly indicates that, though the measurement conditions and set-parameters are same for three different shapes of ZnS nanocrystals, the nanocrystal shape is important for the observed rectification behavior. It has been well known that the nanocrystal shape, aspect ratio, crystalline quality, and radius of curvature at the tip of the nanomaterials play significant role in field emitting property of nanocrystals.[9−11,15] Additionally, the nanostructures with vertically aligned structures with large aspect ratio and sharp edge at the tip believed to have improved field emission properties.[11] Our STS measurements and FN curves on different shaped ZnS nanocrystals also suggest that the field emission is dominating in 1D nanostructures and it is less significant for symmetric spherical nanodots. Comparison of FN curves plotted at negative and positive bias for ZnS nanorod and nanowire shows that the magnitude of $\ln(I/V^2)$, which is sensitive to the magnitude of tunneling current, beyond the logarithmic region of FN plot, is greater for negative bias indicating the FN tunneling is dominating at the negative bias (Supporting Information, Figure S9).

In DBTJ configuration, the width of $J_{\text{Tip-nanocrystal}}$ and $J_{\text{nanocrystal-HOPG}}$ junctions defines the voltage drop across the two junctions and height of the barrier is defined by the capping molecules at both the junctions. Additionally, at finite external bias voltages, majority of the voltage drops at $J_{\text{Tip-nanocrystal}}$ and $J_{\text{nanocrystal-HOPG}}$ junctions due to the insulating behavior of capping molecules.[48,49] However, a fraction of voltage should drop across the inorganic core of ZnS nanocrystal due to its dielectric nature (dielectric constant, $\varepsilon_r \sim 9.5$). Such voltage distribution leans the conduction and valence levels of ZnS nanocrystal in a direction opposite to the external electric field forming a trapezoidal barrier across the ZnS nanocrystal with respect to the $E_{\text{F-HOPG}}$ and $E_{\text{F-Tip}}$. At zero bias, no net tunneling of electrons could occur through the ZnS nanocrystal owing to the near equal energies of $E_{\text{F-HOPG}}$ and $E_{\text{F-Tip}}$ (Figure 5a). At low negative bias voltage ($<V_{\text{trans}}$), the electrons participate in the direct tunneling through the sub-gap region of ZnS nanocrystal resulting in a low degree of tunneling current (regime I, Figure 4a). At higher negative bias voltage, resonant tunneling of electrons takes place through the first few conduction levels of ZnS nanocrystal revealing the evolution of peak-like behavior in the dI/dV spectra (Figure 3g−i and regime II in Figure 4b). Further increased bias voltage (≥1.6 V) initiates the FN tunneling of electrons through the triangular barrier formed by the leaned conduction levels enabling the field emission from ZnS nanorod or nanowire (regime III in Figure 4b and Figure 5b). On the other hand, at low positive bias voltage, direct tunneling of electrons through sub-gap region of ZnS nanocrystal results in the low degree of tunneling current. At higher positive voltages, electrons participate in the resonant tunneling from the tip to substrate through the valence levels of ZnS nanocrystal. Further increase of positive bias voltage cannot initiate the field emission through the ZnS nanocrystal as the high resistance associated with the tunneling of electrons while tunneling through filled states of the ZnS nanocrystal (Figure 5c). Therefore, at positive bias a lesser magnitude of tunneling current is observed in comparison to the large tunneling current in negative bias enabling the rectification effect from the ZnS nanorod or nanowire. Absence of field emission from the ZnS nanodot may associate with spherical nature of the dot. In general, the nanocrystals with large aspect ratio have been proved to show improved field emission properties due to its sharp morphology at the edge of the tip. Also, the sharpness at the tip edge of a nanocrystal believed has profound effect on the turn-on voltage for field emission with low values for sharper nanocrystals. Additionally, the increase in the length of a nanocrystal enhances the field emission intensity with low turn on fields for sharper nanocrystals. In contrary, the spherical shaped nanocrystals are not favorable for field emission due to its reduced aspect ratio or it needs high applied voltages to initiate the field emission owing to its large diameter. The ZnS nanodot may require more external voltages to initiate the FN tunneling mechanism owing to its large size and radius of curvature in comparison to that of nanorod or nanowire.

We have calculated the rectification ratio (RR) at different set-voltages for a particular set-current for quantitative comparison of rectification behavior of ZnS nanodots, nanorods, and nanowires. The RR is defined by the ratio of magnitude of tunneling current measured at bias-voltage of −2.5 V to the tunneling current measured at bias-voltage of +2.5 V. The $I-V$ measurements on ZnS nanodots suggest RR near to one at all the bias voltages (Figure 6). The RR becomes

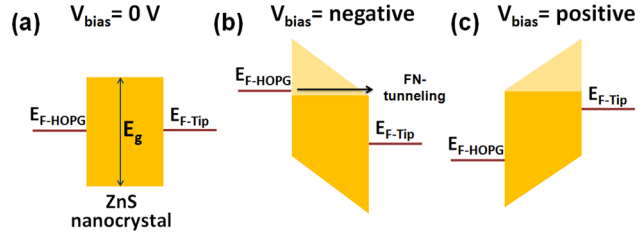

Figure 5. Schematic presentation of electron tunneling processes through ZnS nanocrystal (a) at zero bias, (b) at negative bias, and (c) at positive bias. At low negative bias, direct tunneling of the electrons from HOPG to tip occurs through the sub-gap (E_g) region of ZnS nanocrystal until the Fermi level of HOPG lines up with the first conduction level of ZnS nanocrystal. At high negative bias, resonant tunneling is favorable through the conduction levels of the nanocrystal. A further increase in the voltage initiates FN tunneling phenomenon through the triangular barrier (shaded region in the scheme b) formed across the ZnS nanorod or nanowire resulting in large tunneling current. At positive bias, the field emission is not favorable through the valence channels as the large resistance offered to the electrons through filled states of the ZnS nanocrystal.

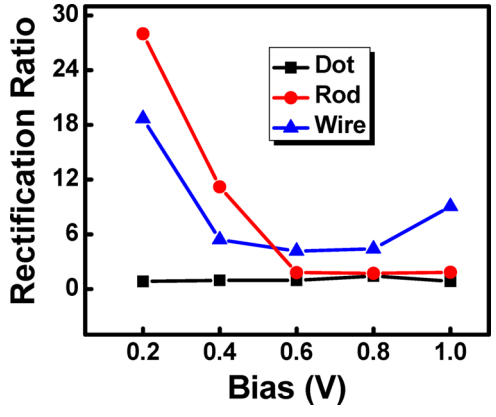

Figure 6. Plot of rectification ratio (RR) of ZnS nanodot (black square and line), nanorod (red dot and line), and nanowire (blue triangle and line) for different set-voltages (0.2 V, 0.4 V, 0.6, 0.8, and 1.0 V) measured at fixed set-current of 0.1 nA.

dx.doi.org/10.1021/am501165p | ACS Appl. Mater. Interfaces 2014, 6, 7856−7863

pronounced with the decrement of set-voltage for a fixed set-current for both nanorods and nanowires. The tip will be in closer proximity of the nanorod or nanowire at low set-voltages compared to the higher set-voltage for a fixed set-current, which further increases the asymmetry in the voltage distribution at $J_{\text{Tip-nanocrystal}}$ and $J_{\text{nanocrystal-HOPG}}$ junctions affecting the RR ratio (Figure 6). Gradual increase of tip to nanorod/nanowire distance by increasing the set voltage (0.2 V to 1 V) at a fixed set current (0.1 nA) allows the symmetric voltage distribution at $J_{\text{Tip-nanocrystal}}$ and $J_{\text{nanocrystal-HOPG}}$ leading to the reduced RR at higher set-voltages (Figure 6). Our measurements reveal that RR is the highest for ZnS nanorod followed by the nanowire. The observation of high rectification ratio for nanorods may be effect of larger conductivity in comparison to that of nanowires, where the probable charge relaxation mechanism along the length of the nanowire may hinders the RR.

CONCLUSIONS

In conclusion, we have demonstrated the shape dependent synthesis of ZnS nanocrystals into nanodots, nanorods, and nanowires. We demonstrate shape dependent current rectification behavior from 1D ZnS nanocrystal using STM and STS technique. We proposed a tunneling mechanism where direct tunneling followed by resonant tunneling mechanism of electrons is dominant through ZnS nanocrystal at low positive and negative bias voltages. We further identified that field emission of electrons in FN tunneling regime is dominated through ZnS nanorod and nanowire at higher negative bias voltages. Therefore, the performance of single nanorod or nanowire based rectifier is dominated by the transition of tunneling mechanism into FN tunneling at large input bias voltages. Generally, the field emission property depends on the radius of curvature and work function of the material. The radius of curvature of our ZnS nanorod or nanowire is less than 2 nm at the surface, which is much less than the radius of curvature of the conventional field emitting nanomaterials. Understanding the tunneling mechanism for the origin of rectification from a single nanorod or nanowire could provide a means for realizing miniaturized device.

ASSOCIATED CONTENT

Supporting Information

TEM and HRTEM images of ZnS nanodots, line profiles of HRTEM images, UV–vis absorption spectra of different shapes of ZnS nanocrystals, comparison of XRD of ZnS nanocrystals synthesized using different capping ligands, STM and STS on bare HOPG substrate, bulk band diagram of ZnS, schematic of tip-nanocrystal-substrate configuration, comparison of FN plots at positive and negative bias voltages for ZnS nanodot, nanorod, and nanowire. This material is available free of charge via the Internet at http://pubs.acs.org/.

AUTHOR INFORMATION

Corresponding Author

*Email: camsa2@iacs.res.in.

Notes

The authors declare no competing financial interest.

ACKNOWLEDGMENTS

Financial support from DST, India, is gratefully acknowledged. U. Thupakula and A. Dalui acknowledge CSIR, India, for fellowships.

REFERENCES

(1) Peng, X.; Manna, L.; Yang, W.; Wickham, J.; Scher, E.; Kadavanich, A.; Alivisatos, A. P. Shape Control of CdSe Nanocrystals. *Nature* **2000**, *404*, 59–61.

(2) Buhro, W. E.; Colvin, V. L. Semiconductor Nanocrystals: Shape Matters. *Nat. Mater.* **2003**, *2*, 138–139.

(3) Jun, Y. W.; Choi, J. S.; Cheon, J. Shape Control of Semiconductor and Metal Oxide Nanocrystals through Nonhydrolytic Colloidal Routes. *Angew. Chem. Int. Ed.* **2006**, *45*, 3414–3439.

(4) Acharya, S.; Kundu, S.; Hill, J. P.; Richards, G. J.; Ariga, K. Nanorod Driven Orientational Control of Liquid Crystal for Polarization Tailored Electro-optic Devices. *Adv. Mater.* **2009**, *21*, 989–993.

(5) Thupakula, U.; Khan, A. H.; Bal, J. K.; Ariga, K.; Acharya, S. Size Selective Excitonic Transition Energies in Strongly Confined CdSe Quantum Dots. *J. Nanosci. Nanotechnol.* **2011**, *11*, 7709–7714.

(6) Khan, A. H.; Thupakula, U.; Dalui, A.; Maji, S.; Debangshi, A.; Acharya, S. Evolution of Long Range Bandgap Tunable Lead Sulfide Nanocrystals with Photovoltaic Properties. *J. Phys. Chem. C* **2013**, *117*, 7934–7939.

(7) Acharya, S.; Sarma, D. D.; Golan, Y.; Sengupta, S.; Ariga, K. Shape Dependent Confinement in Ultrasmall Zero, One, and Two Dimensional PbS Nanostructures. *J. Am. Chem. Soc.* **2009**, *131*, 11282–11283.

(8) Hu, J.; Li, L. S.; Yang, W.; Manna, L.; Wang, L. W.; Alivisatos, A. P. Linearly Polarized Emission from Colloidal Semiconductor Quantum Rods. *Science* **2001**, *292*, 2060–2063.

(9) Shinde, D. R.; Chavan, P. G.; Sen, S.; Joag, D. S.; More, M. A.; Gadkari, S. C.; Gupta, S. K. Enhanced Field Emission from SnO_2:$WO_{2.72}$ Nanowire Heterostructures. *ACS Appl. Mater. Interfaces* **2011**, *3*, 4730–4735.

(10) Fang, X.; Bando, Y.; Gautam, U. K.; Ye, C.; Golberg, D. Inorganic Semiconductor Nanostructures and Their Field Emission Applications. *J. Mater. Chem.* **2008**, *18*, 509–522.

(11) Chang, Y. M.; Liu, M. C.; Kao, P. H.; Lin, C. M.; Lee, H. Y.; Juang, J. Y. Field Emission in Vertically Aligned ZnO/Si-Nanopillars with Ultra-Low Turn-On Field. *ACS Appl. Mater. Interfaces* **2012**, *4*, 1411–1416.

(12) Lin, J.; Huang, Y.; Bando, Y.; Tang, C.; Li, C.; Golberg, D. Synthesis of In_2O_3 Nanowire Decorated Ga_2O_3 Nanobelt Heterostructures and Their Electrical and Field Emission Properties. *ACS Nano* **2010**, *4*, 2452–2458.

(13) Ahmad, M.; Sun, H.; Zhu, J. Enhanced Photoluminescence and Field Emission Behavior of Vertically Well Aligned Arrays of In-Doped ZnO Nanowires. *ACS Appl. Mater. Interfaces* **2011**, *3*, 1299–1305.

(14) Pan, Z.; Lai, H. L.; Au, F. C. K.; Duan, X.; Zhou, W.; Shi, W.; Wang, N.; Lee, C. S.; Wong, N. B.; Lee, S. T.; Xie, S. Oriented Silicon Carbide Nanowires: Synthesis and Field Emission Properties. *Adv. Mater.* **2000**, *12*, 1186–1190.

(15) Warule, S. S.; Chaudhari, N. S.; Ambekar, J. D.; Kale, B. B.; More, M. A. Hierarchical Nanostructured ZnO with Nanorods Engendered to Nanopencils and Pin Cushion Cactus with Its Field Emission Study. *ACS Appl. Mater. Interfaces* **2011**, *3*, 3454–3462.

(16) Nakaya, M.; Shikishima, M.; Shibuta, M.; Hirata, N.; Eguchi, T.; Nakajima, A. Molecular Scale and Wide Energy Range Tunneling Spectroscopy on Self Assembled Monolayers of Alkanethiol Molecules. *ACS Nano* **2012**, *6*, 8728–8734.

(17) Banin, U.; Cao, Y. W.; Katz, D.; Millo, O. Identification of Atomic-like Electronic States in Indium Arsenide Nanocrystal Quantum Dots. *Nature* **1999**, *400*, 542–544.

(18) Liljeroth, P.; Emmichoven, P. A. Z. V.; Hickey, S. G.; Weller, H.; Grandidier, B.; Allan, G.; Vanmaekelbergh, D. Density of States Measured by Scanning Tunneling Spectroscopy Sheds New Light on the Optical Transitions in PbSe Nanocrystals. *Phys. Rev. Lett.* **2005**, *95*, 086801.

(19) Liljeroth, P.; Jdira, L.; Overgaag, K.; Grandidier, B.; Spellerb, S.; Vanmaekelbergh, D. Can Scanning Tunnelling Spectroscopy Measure the Density of States of Semiconductor Quantum Dots? *Phys. Chem. Chem. Phys.* **2006**, *8*, 3845–3850.

(20) Bakkers, E. P. A. M.; Vanmaekelbergh, D. Resonant Electron Tunneling through Semiconducting Nanocrystals in a Symmetrical and an Asymmetrical Junction. *Phys. Rev. B* **2000**, *62*, R7743−R7746.
(21) Beebe, J. M.; Kim, B. S.; Gadzuk, J. W.; Frisbie, C. D.; Kushmerick, J. G. Transition from Direct Tunneling to Field Emission in Metal Molecule Metal Junctions. *Phys. Rev. Lett.* **2006**, *97*, 026801.
(22) Thupakula, U.; Bal, J. K.; Debangshi, A.; Khan, A. H.; Dalui, A.; Acharya, S. Ultra Narrow PbS Nanorod Field Emitter. *J. Phys. Chem. C* **2012**, *116*, 18564−18570.
(23) Kundu, S.; Hill, J. P.; Richards, G. J.; Ariga, K.; Khan, A. H.; Thupakula, U.; Acharya, S. Crystallographic Phase Induced Electro-optic Properties of Nanorod Blend Nematic Liquid Crystal. *J. Nanosci. Nanotechnol.* **2011**, *11*, 7729−7734.
(24) Fang, X.; Bando, Y.; Liao, M.; Gautam, U. K.; Zhi, C.; Dierre, B.; Liu, B.; Zhai, T.; Sekiguchi, T.; Koide, Y.; Golberg, D. Single-Crystalline ZnS Nanobelts as Ultraviolet-Light Sensors. *Adv. Mater.* **2009**, *21*, 2034−2039.
(25) Liu, H.; Hu, L.; Watanabe, K.; Hu, X.; Dierre, B.; Kim, B.; Sekiguchi, T.; Fang, X. Cathodoluminescence Modulation of ZnS Nanostructures by Morphology, Doping, and Temperature. *Adv. Funct. Mater.* **2013**, *23*, 3701−3709.
(26) Fang, X.; Wu, L.; Hu, L. ZnS Nanostructure Arrays: A Developing Material Star. *Adv. Mater.* **2011**, *23*, 585−598.
(27) Hu, L.; Brewster, M. M.; Xu, X.; Tang, C.; Gradečak, S.; Fang, X. Heteroepitaxial Growth of GaP/ZnS Nanocable with Superior Optoelectronic Response. *Nano Lett.* **2013**, *13*, 1941−1947.
(28) Pradhan, N.; Acharya, S.; Ariga, K.; Karan, N. S.; Sarma, D. D.; Wada, Y.; Efrima, S.; Golan, Y. Chemically Programmed Ultrahigh Density Two Dimensional Semiconductor Superlattice Array. *J. Am. Chem. Soc.* **2010**, *132*, 1212−1213.
(29) Zscheckel, T.; Wisniewski, W.; Gebhardt, A.; Rüssel, C. Mechanisms Counteracting the Growth of Large Grains in Industrial ZnS Grown by Chemical Vapor Deposition. *ACS Appl. Mater. Interfaces* **2014**, *6*, 394−400.
(30) Fang, X. S.; Ye, C. H.; Zhang, L. D.; Wang, Y. H.; Wu, Y. C. Temperature-Controlled Catalytic Growth of ZnS Nanostructures by the Evaporation of ZnS Nanopowders. *Adv. Funct. Mater.* **2005**, *15*, 63−68.
(31) Belman, N.; Acharya, S.; Konovalov, O.; Vorobiev, A.; Israelachvili, J.; Efrima, S.; Golan, Y. Hierarchical Assembly of Ultranarrow Alkylamine-Coated ZnS Nanorods: A Synchrotron Surface X-ray Diffraction Study. *Nano Lett.* **2008**, *8*, 3858−3864.
(32) Khan, A. H.; Ji, Q.; Ariga, K.; Thupakula, U.; Acharya, S. Size Controlled Ultranarrow PbS Nanorods: Spectroscopy and Robust Stability. *J. Mater. Chem.* **2011**, *21*, 5671−5676.
(33) Kundu, S.; Hill, J. P.; Richards, G. J.; Ariga, K.; Khan, A. H.; Thupakula, U.; Acharya, S. Ultranarrow PbS Nanorod Nematic Liquid Crystal Blend for Enhanced Electro-optic Properties. *ACS Appl. Mater. Interfaces* **2010**, *2*, 2759−2766.
(34) Alig, A. R. G.; Akbulut, M.; Golan, Y.; Israelachvili, J. Forces between Surfactant-Coated ZnS Nanoparticles in Dodecane: Effect of Water. *Adv. Funct. Mater.* **2006**, *16*, 2127−2134.
(35) Cadars, S.; Smith, B. J.; Epping, J. D.; Acharya, S.; Belman, N.; Golan, Y.; Chmelka, B. F. Atomic Positional Versus Electronic Order in Semiconducting ZnSe Nanoparticles. *Phys. Rev. Lett.* **2009**, *103*, 136802.
(36) Hens, Z.; Vanmaekelbergh, D.; Stoffels, E. J. A. J.; Kempen, H. V. Effects of Crystal Shape on the Energy Levels of Zero Dimensional PbS Quantum Dots. *Phys. Rev. Lett.* **2002**, *88*, 236803.
(37) Cai, J.; Ruffieux, P.; Jaafar, R.; Bieri, M.; Braun, T.; Blankenburg, S.; Muoth, M.; Seitsonen, A. P.; Saleh, M.; Feng, X.; Mullen, K.; Fasel, R. Atomically Precise Bottom-Up Fabrication of Graphene Nanoribbons. *Nature* **2010**, *466*, 470−473.
(38) Steiner, D.; Mokari, T.; Banin, U.; Millo, O. Electronic Structure of Metal Semiconductor Nanojunctions in Gold CdSe Nanodumbbells. *Phys. Rev. Lett.* **2005**, *95*, 056805.
(39) Steinberg, H.; Lilach, Y.; Salant, A.; Wolf, O.; Faust, A.; Millo, O.; Banin, U. Anomalous Temperature Dependent Transport through Single Colloidal Nanorods Strongly Coupled to Metallic Leads. *Nano Lett.* **2009**, *9*, 3671−3675.
(40) Steiner, D.; Azulay, D.; Aharoni, A.; Salant, A.; Banin, U.; Millo, O. Electronic Structure and Self Assembly of Cross Linked Semiconductor Nanocrystal Arrays. *Nanotechnology* **2008**, *19*, 065201.
(41) Urazhdin, S.; Bilc, D.; Tessmer, S. H.; Mahanti, S. D.; Kyratsi, T.; Kanatzidis, M. G. Scanning Tunneling Microscopy of Defect States in the Semiconductor Bi_2Se_3. *Phys. Rev. B* **2002**, *66*, 161306.
(42) Alperson, B.; Rubinstein, I.; Hodes, G. Identification of Surface States on Individual CdSe Quantum Dots by Room Temperature Conductance Spectroscopy. *Phys. Rev. B* **2001**, *63*, 081303.
(43) Feenstra, R. M.; Stroscio, J. A.; Fein, A. P. Tunneling Spectroscopy of the Si(111) 2 × 1 Surface. *Surf. Sci.* **1987**, *181*, 295−306.
(44) Jo, G.; Na, S. I.; Oh, S. H.; Lee, S.; Kim, T. S.; Wang, G.; Choe, M.; Park, W.; Yoon, J.; Kim, D. Y.; Kahng, Y. H.; Lee, T. Tuning of a Graphene Electrode Work Function to Enhance the Efficiency of Organic Bulk Heterojunction Photovoltaic Cells with an Inverted Structure. *Appl. Phys. Lett.* **2010**, *97*, 213301.
(45) Thupakula, U.; Bal, J. K.; Dalui, A.; Debangshi, A.; Sarma, D. D.; Acharya, S. Current Rectification by a Single ZnS Nanorod Probed Using a Scanning Tunneling Microscopic Technique. *J. Mater. Chem. C* **2014**, *2*, 1158−1164.
(46) Katz, D.; Millo, O.; Kan, S. H.; Banin, U. Control of Charging in Resonant Tunneling Through InAs Nanocrystal Quantum Dots. *Appl. Phys. Lett.* **2001**, *79*, 117−119.
(47) Bernard, R.; Comtet, G.; Dujardin, G.; Huc, V.; Mayne, A. J. Imaging and Spectroscopy of Individual CdSe Nanocrystals on Atomically Resolved Surfaces. *Appl. Phys. Lett.* **2005**, *87*, 053114.
(48) Talapin, D. V.; Murray, C. B. PbSe Nanocrystal Solids for n- and p-Channel Thin Film Field Effect Transistors. *Science* **2005**, *310*, 86−89.
(49) Medintz, I. L.; Uyeda, H. T.; Goldman, E. R.; Mattoussi, H. Quantum Dot Bioconjugates for Imaging, Labelling, and Sensing. *Nat. Mater.* **2005**, *4*, 435−446.